Simulating Gyrokinetic Microinstabilities in Stellarator Geometry with GS2

J. A. Baumgaertel,[1] E. A. Belli,[2] W. Dorland,[3] W. Guttenfelder,[1] G. W. Hammett,[1] D. R. Mikkelsen,[1] G. Rewoldt,[1] W. M. Tang,[1] and P. Xanthopoulos[4]

[1)] *Princeton Plasma Physics Laboratory, Princeton, New Jersey 08543*

[2)] *General Atomics, San Diego, California 92186*

[3)] *University of Maryland, College Park, Maryland 20742*

[4)] *Max-Planck-Institut fuer Plasmaphysik, D-17491 Greifswald, Germany*

(Dated: 19 September 2011)

The nonlinear gyrokinetic code GS2 has been extended to treat non-axisymmetric stellarator geometry. Electromagnetic perturbations and multiple trapped particle regions are allowed. Here, linear, collisionless, electrostatic simulations of the quasi-axisymmetric, three-field period National Compact Stellarator Experiment (NCSX) design QAS3-C82 have been successfully benchmarked against the eigenvalue code FULL. Quantitatively, the linear stability calculations of GS2 and FULL agree to within $\sim 10\%$.

I. INTRODUCTION

One of the most important issues for magnetic fusion is the confinement of heat and particles. Turbulent transport (most likely the result of drift wave instabilities) causes a significant amount of heat loss in tokamaks and spherical tori.[1] Neoclassical transport, on the other hand, can often account for the poor confinement in traditional stellarators.[2] However, modern stellarator designs, such as Wendelstein 7-AS (W7-AS),[3] Wendelstein 7-X (W7-X),[4,5] the National Compact Stellarator Experiment (NCSX),[6] the Large Helical Device (LHD)[7], and the Helically Symmetric Experiment (HSX)[8–10] have shown or are designed to have improved neoclassical confinement and stability properties. Understanding plasma turbulence and transport could further improve the performance of stellarators. Progress in design of stellarators for optimal transport has been made by coupling the gyrokinetic code GENE[33] with the configuration optimization code STELLOPT.[11,12]

Gyrokinetic studies of drift-wave-driven turbulence in stellarator geometry are relatively recent and comprehensive scans are scarce. Most of these studies were done using upgraded versions of well-established axisymmetric codes which include comprehensive kinetic dynamics (multispecies, collisions, finite beta) to the more general case of non-axisymmetric stellarator geometry, in the flux tube limit. The first non-axisymmetric linear gyrokinetic stability studies, for both the ion-temperature-gradient-driven (ITG) mode and the trapped-electron mode (TEM), were done with the linear eigenvalue FULL code,[13–15] including a comparison of stability in nine stellarator configurations.[16] Extensive studies have been done with the upgraded GENE code, including the first nonlinear gyrokinetic simulations.[17] More recently, the GKV-X code, which uses the adiabatic electron approximation, has been used to analyze linear ITG modes and zonal flows in LHD and nonlinear studies are in progress.[18]

For this purpose, the axisymmetric nonlinear microinstability code GS2[19] has been extended to treat the more general case of non-axisymmetric stellarator geometry. GS2 contains a full (except that the equilibrium distribution function is taken to be a Maxwellian) implementation of the 5-D Frieman and Chen nonlinear gyrokinetic equation in the flux tube limit,[19,20] with an efficient parallelization for modern supercomputers.[27] It treats electrons and an arbitrary number of ion species on an equal footing, and includes trapped particles, electromagnetic perturbations, and a momentum-conserving pitch-angle-scattering collision operator. The extension of the code to non-axisymmetric geometry not only retains all of

the above dynamics of the axisymmetric version, but also allows, most importantly, multiple trapped particle regions and multiple totally-trapped pitch angles at a given theta grid point. (By "totally-trapped," we mean particles with such a small parallel velocity that they are limited to one grid point at the bottom of a well.) Tokamaks only have one trapped particle region, but as stellarators can have many deep, narrow magnetic wells which can trap particles (though NCSX has only a single deep well, with other shallow wells, and is a bridge in configuration space between tokamaks and other stellarators). In order to treat the trapped particles accurately, one needs to resolve these wells sufficiently with high grid resolution. With the GS2 modifications, we allow for more flexible, decoupled pitch angle and parallel spatial grids, relative to the original GS2 algorithm which required every grid point (θ_j) along the field line to correspond exactly to the turning point of trapped pitch angle ($\lambda_i = \mu/E$) grid points.[27]

Beyond these extensions, a GS2 stellarator simulation requires different geometry codes to build its input grids than standard tokamak runs. For these non-axisymmetric simulations, the geometrical coefficients are based on a VMEC[21,22] 3D MHD equilibrium, which is transformed into Boozer coordinates[23] by the TERPSICHORE code.[24] From this equilibrium, the VVBAL code[25] constructs data along a chosen field line necessary for the microinstability calculations: $B = |\mathbf{B}|$, the $\nabla\mathbf{B}$ drift, the curvature drift, and the metric coefficients. While these extensions were used to study HSX plasmas,[26] here we verify the non-axisymmetric extension of GS2 through comparisons with FULL on NCSX plasmas. Good agreement between the GS2 code and the FULL code in the axisymmetric limit has been extensively demonstrated previously.[27,28] While the non-axisymmetric upgrade of GS2 retains the nonlinear dynamics, in these studies we focus on systematic scans of gyrokinetic linear stability.

The organization of this paper is as follows. The NCSX equilibrium used for the benchmark is described in Section II. Comparisons between the GS2 code and the FULL code in non-axisymmetric geometry over a range of parameters including $\eta = L_n/L_T$ (where L_n is the density gradient scale length and L_T is the temperature gradient scale length), $k_y\rho_i$, T_i/T_e, and geometrical coordinates are presented in Section III. Further results using the GS2 code to investigate effects of density and temperature gradients are presented in Section IV. Conclusions and a discussion of future work are given in Section V. Finally, Appendix A contains definitions of the normalizations and radial coordinate used by GS2.

II. THE QAS3-C82 EQUILIBRIUM

All of the benchmark calculations use a VMEC equilibrium based on a 1999 NCSX design known as QAS3-C82,[12] which is shown in Figure 1. This configuration is quasi-axisymmetric with three field periods. It has an aspect ratio of 3.5 and a major radius of 1.4 m. NCSX was designed to have good neoclassical transport and MHD stability properties and good drift trajectories similar to those in tokamaks. Strong axisymmetric components of shaping provide good ballooning stability properties at lower aspect ratio. Furthermore, the QAS3-C82 equilibrium has a monotonically increasing rotational transform profile which provides stability to neoclassical tearing modes across the entire cross section.[12,29]

For most of these runs, we chose the surface at $s = 0.875$ ($s \sim \langle (r/a)^2 \rangle$ is the normalized toroidal flux) and the field line at $\alpha = \pi/3$ ($\alpha = \zeta - q\theta$; ζ is the Boozer toroidal angle, θ is the Boozer poloidal angle). The cross-section at this point is the crescent shape, seen in Figure 17 of Ref. 30. The coordinate along the field line is θ, the poloidal angle. At this surface, the safety factor $q = 2.118$ and the average β (the ratio of the plasma pressure to the magnetic pressure) is $\langle \beta \rangle = 0.01\%$. Lastly, the ballooning parameter[25] is $\theta_0 = 0$, except in Figure 6.

Figure 2 shows the variation of the magnitude of the magnetic field along a chosen magnetic field line. Resolution studies for the spatial grid used in the GS2 runs indicate that 330 theta grid points per poloidal period and about 90 pitch angles ($\lambda = \mu/E$) showed convergence in the growth rate to within 2%, however $< 10\%$ error is possible with coarser grids. It was also found that a θ range extending from -3π to 3π was sufficient for a typical simulation grid, meaning that the eigenfunctions for the modes decayed to insignificant values before reaching these boundaries. (The endpoints of $B(\theta)$ were increased slightly, by less than 1%, to be global maxima, per normal GS2 operations.)

The equilibrium's geometry suggests unstable drift waves exist. The variations of $(k_\perp/n)^2$, where n is the toroidal mode number, and the curvature drift along the same chosen field line can be seen in Figures 3 and 4. By convention, positive curvature drifts are "bad" or destabilizing, while negative curvature drifts are "good" or stabilizing. Significant unstable modes occur where $k_\perp$ is small, which is near $\theta = 0$ for this equilibrium, since instabilities are generally suppressed at large $k_\perp$ by FLR averaging. Also, because Figure 4 indicates that the curvature is bad in this region near $\theta = 0$, it is expected that unstable modes will

appear here.

III. BENCHMARKS WITH FULL

Comparisons between the GS2 code and the FULL code in non-axisymmetric geometry over a range of parameters using the QAS3-C82 equilibrium show linear agreement for our standard case, whose local parameters are shown in Table I. The product of the perpendicular wave number and the gyroradius at $\theta = 0$, $k_y\rho_i$, is 0.3983 (where the toroidal mode number $n = 25$; see App. A) for all cases unless otherwise specified. The standard case is relatively close to the edge, which accounts for the low values of ion temperature, T_i, electron temperature, T_e, and relatively large values for the gradients. The parameter, $\eta = L_n/L_T$ is usually $\eta = 3$, placing most of our studies in an ITG regime (see Figure 7). Correspondingly, $a_N/L_{ni} = a_N/L_{ne} = 13.096$ and $a_N/L_{Ti} = a_N/L_{Te} = 39.288$. The major radius is approximately $R \approx 1.4m$. The normalizing scale length is $a_N = n/k_\perp(\theta = 0) = 0.352m$, not the minor radius, and is described in detail in App. A. These studies are done with electrons and deuterium ions.

Previously, FULL scans showed that the largest linear growth rate occurs at flux surface label $s = 0.875$ (corresponding to a minor radius of $r/a \approx \sqrt{s} \approx 0.94$), for $\alpha = \pi/3$ and $\theta_0 = 0$. GS2 and FULL scans over α and θ_0 (Figures 5 and 6) adopted this s value. The toroidal mode number, n, was fixed at 25 (thus, $k_y\rho_i = \frac{n}{a_N}\rho_i$ varied for each data point, because from App. A, $a_N = 1/|\nabla\alpha|$ and $\rho_i \propto 1/B_a$ vary). These figures indicate good agreement between the GS2 code and the FULL code. The maximum growth rate in Figure 5 occurs for $\alpha = \pi/3$, and GS2 and FULL agree well around this value. In Figure 6, GS2 and FULL again agree well around the growth rate peak at $\theta_0 = 0$.

In all further calculations presented in this paper, $s = 0.875$, $\alpha = \pi/3$ and $\theta_0 = 0$, the location of the maximum growth rate.

We used GS2 to find the instability growth rate dependence on $\eta = L_n/L_T$ and compared it with FULL. The total pressure gradient was kept fixed to maintain consistency with the MHD equilibrium. Both codes found large growth rates at low η (high density gradient) and high η (high temperature gradient) (Figure 7), and agree well, though it can be seen in the frequencies that GS2 found a mode switch earlier than FULL. This can happen since GS2 automatically finds the most unstable mode, whereas FULL usually finds

the mode closest to the initial guess provided to the root finder. In fact, there are three distinct eigenmodes within these regimes of η: at small η, even-symmetry TEM modes dominate; at medium η, odd-symmetry TEM modes dominate; and at larger values of η, an even-symmetry ITG-driven mode dominates[15] (Figure 8). This is typical of an equivalent axisymmetric configuration.[31]

Benchmarks with FULL for scans over T_i/T_e, shown in figure 9, were also successful. For this scan, T_e was varied while T_i was kept constant at $1keV$. As T_i/T_e increases, at this very large value of $R/L_{T_i} \approx 157$, the linear growth rate falls slowly due, most likely, to an enhancement of shielding by adiabatic electrons at large $\sqrt{T_i/T_e}$. This is a very well-known phenomenon in tokamaks.

Comparison scans over $k_y\rho_i$ for $\eta = 0$ and $\eta = 3$ are shown in figure 10. For the $\eta = 0$ curve, the dominating eigenmodes are even in the ranges $0.1 < k_y\rho_i < 0.2$ and $0.6 < k_y\rho_i < 1.1$. Overall, the results from the GS2 code and the FULL code agree well; growth rates differ by at most $\sim 10\%$ except at transitions between modes.

We found high frequency, electron-temperature-gradient-driven (ETG) modes with GS2 at short wavelengths (Figure 11) in the extended $k_y\rho_i$ spectrum for the case of $\eta = 3$. This was not checked with FULL.

IV. CRITICAL GRADIENTS FOR LINEAR INSTABILITY

GS2 was also used to search for critical density gradients and temperature gradients; i.e. to see whether gradients exist at which all drift wave modes are stabilized. Note that for the next series of figures, the normalizing length for the density and temperature gradient length scales is defined as $a_N = (n/k_\perp)(\theta = 0) \sim 0.352m$ (see App. A).

Figure 12 shows a scan over the density gradient at various ion and electron temperature gradients. The results are inconsistent with the equilibrium pressure gradient, as the density gradient was increased at constant temperature gradient. However, because the equilibrium beta is so small ($\sim 0.01\%$), the effect of the variation of the pressure gradient is negligible. We see that there is no nonzero critical density gradient threshold, even in the absence of temperature gradients. There are switches in eigenmode symmetry from even to odd as a_N/L_n increases, or all a_N/L_T values.

However, a critical ion temperature gradient for an ITG-driven mode was found at

$a_N/L_{Ti} \sim 2$ (or $\frac{R}{L_{T_i}} = \frac{R}{a_N}\frac{a_N}{L_{T_i}} \approx 4\frac{a_N}{L_{T_i}} = 8$) in the absence of all other gradients (Figure 13). Likewise, a critical electron temperature gradient for a TEM-driven mode was found at $\frac{a_N}{L_{T_e}} \sim 2$ in the absence of all other gradients (Figure 14).

V. CONCLUSIONS

The nonlinear gyrokinetic code GS2 has been extended to treat non-axisymmetric stellarator geometry. Geometric quantities required for the gyrokinetic simulations are calculated from a VMEC-generated equilibrium using the VVBAL code and are further described in App. A.

Linear, collisionless, electrostatic simulations of the quasi-axisymmetric, three-field period NCSX stellarator design QAS3-C82 have been successfully benchmarked with the eigenvalue code FULL for scans over a range of parameters including η, $k_y\rho_i$, T_i/T_e, α, and θ_0. Quantitatively, the linear stability calculations of GS2 and FULL agree to within about 10% of the mean, except at transitions between modes. Further results using only GS2 included short wavelength modes, odd parity, faster growing modes, and the effect of individual density and temperature gradients.

Future work will include the exploration of the effects of collisionality and electromagnetic dynamics, investigation of finite beta equilibria, and, most significantly, the effects of nonlinear dynamics. A benchmark of stellarator studies is underway between GS2 and the continuum gyrokinetic code GENE[33] for NCSX, as well as stellarators W7-AS and W7-X.

GIST[34] is now capable of creating GS2 geometry data files and will be used in the future, along with the new GS2 grid generator.

ACKNOWLEDGMENTS

The authors would like to thank Dr. L.-P. Ku and Dr. W. A. Cooper for providing equilibrium results from the VMEC and TERPSICHORE codes as well as the resulting parameters from the VVBAL code. Also, thank you to M. A. Barnes for useful discussion.

This work was supported by the U.S. Department of Energy through the SciDAC Center for the Study of Plasma Microturbulence and the Princeton Plasma Physics Laboratory by DOE Contract No. DE-AC02-09CH11466, and by a DOE Fusion Energy Sciences Fellowship.

Appendix A: Geometry Details

In order to make the simulation grid for these GS2 stellarator runs, VMEC creates the 3-D MHD equilibrium, TERPSICHORE transforms it into Boozer coordinates, and VVBAL calculates necessary geometric coefficients along a specified field line. Then, GS2's grid generator, Rungridgen, creates the final grid for use in the microinstability calculations. (A new grid generator is in production, which will be used for further GS2 stellarator calculations.) The normalizations of geometric quantities change between these codes, and knowing them in detail is required for benchmarks between gyrokinetic codes. We define the normalizing length, a_N, in App. A.2.

In GS2, the field-aligned coordinate system is (ρ, α, θ). θ is the poloidal angle and distance along the field line. The magnetic field takes the form $\mathbf{B} = \nabla\alpha \times \nabla\Psi$, where $\alpha = \zeta - q\theta$ is the field line label. The radial coordinate, ρ, can differ between codes, and we define it in App. A.1. More details of general geometry for GS2 are documented in App. A of Ref. 35.

1. Radial coordinate, ρ

VMEC and TERPSICHORE use the normalized toroidal flux surface label $s = \Phi/\Phi_{edge} \sim \langle (r/a)^2 \rangle$ as the radial coordinate, ρ. In the customized version of VVBAL used here, the radial coordinate is transformed to $\rho = \Psi_N = \Psi/(a_N^2 B_a)$, where Ψ_N is the normalized poloidal flux.

Because Rungridgen uses VVBAL output without modification, here $d\rho/d\psi_N \equiv 1$. (In Ref. 35, the definition of the geometry coefficients include the variable $d\rho/d\psi_N$, which can be used to choose the radial coordinate.)

2. Normalizing Quantities, B_a and a_N

The normalizing magnetic field is $B_a = \langle B \rangle$, where $\langle B \rangle$ is a theta-average, not weighted to be a flux-surface average (Ref. 35 chooses B_a differently).

The normalizing length is a_N, given for these calculations by VVBAL as

$$a_N = \frac{n}{\sqrt{|\mathbf{k}_\perp|^2(\theta = 0, \theta_0 = 0)}} = \frac{1}{|\nabla\alpha|}. \tag{A1}$$

GS2 treats perturbed quantities as $A = \hat{A}(\theta) exp(iS)$, where $\mathbf{k}_\perp = \nabla S = n\nabla(\alpha + q\theta_0) = n\nabla[\zeta - q(\theta - \theta_0)]$; n is the toroidal mode number. (In non-axisymmetric devices, n is not a conserved quantum number, because toroidal variations in the equilibrium give coupling between n modes. However, in the small-$\rho*$, high-n limit, this coupling is weak, and n can just be considered a coefficient to select a particular value of $k_\perp$.)

In the notation of Eqn. A.11 of App. A in Ref. 35,

$$|\mathbf{k}_\perp|^2 = |\nabla S|^2 = k_\theta^2 \left| g_1 + 2\theta_0 g_2 + \theta_0^2 g_3 \right| \tag{A2}$$

where g_1, g_2, and g_3 are coefficients in the geometry file written by VVBAL and read by GS2. Also, $k_\theta = k_y = n/a_N$. (The GS2 variable `aky` is defined as $k_y \rho_i$, with $\rho_i \propto 1/B_a$.)

In the notation of Eqn. 7 of Ref. 34,

$$|\mathbf{k}_\perp|^2 = n^2 \frac{\sqrt{g} B^2}{\Psi'^2(s)} [C_p + C_s(\theta - \theta_0) + C_q(\theta - \theta_0)^2], \tag{A3}$$

where $\sqrt{g}$ is the Jacobian, C_p, C_s, and C_q are defined in section II of Ref. 34.

So, VVBAL writes:

$$g_1 = a_N^2 \frac{\sqrt{g} B^2}{\Psi'^2(s)} [C_p + C_s\theta + C_q\theta^2] \tag{A4}$$

$$g_2 = -a_N^2 \frac{\sqrt{g} B^2}{\Psi'^2(s)} \left[C_q\theta + \frac{C_s}{2} \right] \tag{A5}$$

$$g_3 = a_N^2 \frac{\sqrt{g} B^2}{\Psi'^2(s)} C_q \tag{A6}$$

REFERENCES

[1] P. C. Liewer, Nuclear Fusion **25**, 543 (1985).

[2] G. Fu, M. Isaev, L. Ku, M. Mikhailov, M. H. Redi, R. Sanchez, A. Subbotin, W. A. Cooper, S. P. Hirshman, D. Monticello, A. Reiman, and M. Zarnstorff, Fusion Science and Technology **51**, 218 (2007).

[3] J. Sapper and H. Renner, Fusion Technology **7**, 62 (1990).

[4] C. Beidler, G. Grieger, F. Herrnegger, E. Harmeyer, J. Kisslinger, W. Lotz, H. Maassberg, P. Merkel, J. Nuhrenberg, F. Rau, J. Sapper, F. Sardei, R. Scardovelli, A. Schluter, and H. Wobig, Fusion Technology **17**, 148 (1990).

[5]G. Grieger, W. Lotz, P. Merkel, J. Nuhrenberg, J. Sapper, E. Strumberger, H. Wobig, R. Burhenn, V. Erckmann, U. Gasparino, L. Giannone, H. J. Hartfuss, R. Jaenicke, G. Kuhner, H. Ringler, A. Weller, F. Wagner, the W7-X Team, and the W7-AS Team, Physics of Fluids B: Plasma Physics **4**, 2081 (1992).

[6]M. C. Zarnstorff, L. A. Berry, A. Brooks, E. Fredrickson, G. Fu, S. Hirshman, S. Hudson, L. Ku, E. Lazarus, D. Mikkelsen, D. Monticello, G. H. Neilson, N. Pomphrey, A. Reiman, D. Spong, D. Strickler, A. Boozer, W. A. Cooper, R. Goldston, R. Hatcher, M. Isaev, C. Kessel, J. Lewandowski, J. F. Lyon, P. Merkel, H. Mynick, B. E. Nelson, C. Nuehrenberg, M. Redi, W. Reiersen, P. Rutherford, R. Sanchez, J. Schmidt, and R. B. White, Plasma Physics and Controlled Fusion **43**, A237 (2001).

[7]H. Yamada, A. Komori, N. Ohyabu, O. Kaneko, K. Kawahata, K. Y. Watanabe, S. Sakakibara, S. Murakami, K. Ida, R. Sakamoto, Y. Liang, J. Miyazawa, K. Tanaka, Y. Narushima, S. Morita, S. Masuzaki, T. Morisaki, N. Ashikawa, L. R. Baylor, W. A. Cooper, M. Emoto, P. W. Fisher, H. Funaba, M. Goto, H. Idei, K. Ikeda, S. Inagaki, N. Inoue, M. Isobe, K. Khlopenkov, T. Kobuchi, A. Kostrioukov, S. Kubo, T. Kuroda, R. Kumazawa, T. Minami, S. Muto, T. Mutoh, Y. Nagayama, N. Nakajima, Y. Nakamura, H. Nakanishi, K. Narihara, K. Nishimura, N. Noda, T. Notake, S. Ohdachi, Y. Oka, M. Osakabe, T. Ozaki, B. J. Peterson, G. Rewoldt, A. Sagara, K. Saito, H. Sasao, M. Sasao, K. Sato, M. Sato, T. Seki, H. Sugama, T. Shimozuma, M. Shoji, H. Suzuki, Y. Takeiri, N. Tamura, K. Toi, T. Tokuzawa, Y. Torii, K. Tsumori, T. Watanabe, I. Yamada, S. Yamamoto, M. Yokoyama, Y. Yoshimura, T. Watari, Y. Xu, K. Itoh, K. Matsuoka, K. Ohkubo, T. Satow, S. Sudo, T. Uda, K. Yamazaki, O. Motojima, and M. Fujiwara, Plasma Physics and Controlled Fusion **43**, A55 (2001).

[8]S. P. Gerhardt, J. N. Talmadge, J. M. Canik, and D. T. Anderson, Physical Review Letters **94**, 015002 (2005).

[9]J. M. Canik, D. T. Anderson, F. S. B. Anderson, K. M. Likin, J. N. Talmadge, and K. Zhai, Physical Review Letters **98**, 085002 (2007).

[10]J. N. Talmadge, F. S. B. Anderson, D. T. Anderson, C. Deng, W. Guttenfelder, K. M. Likin, J. Lore, J. C. Schmitt, and K. Zhai, Plasma and Fusion Research **3**, S1002 (2008).

[11]H. E. Mynick, N. Pomphrey, and P. Xanthopoulos, Physical Review Letters **105**, 095004 (2010).

[12]A. Reiman, G. Fu, S. Hirshman, L. Ku, D. Monticello, H. Mynick, M. Redi, D. Spong,

M. Zarnstorff, B. Blackwell, A. Boozer, A. Brooks, W. A. Cooper, M. Drevlak, R. Goldston, J. Harris, M. Isaev, C. Kessel, Z. Lin, J. F. Lyon, P. Merkel, M. Mikhailov, W. Miner, G. Neilson, M. Okamoto, N. Pomphrey, W. Reiersen, R. Sanchez, J. Schmidt, A. Subbotin, P. Valanju, K. Y. Watanabe, R. White, N. Nakajima, and C. Nuehrenberg, Plasma Physics and Controlled Fusion **41**, B273 (1999).

[13]G. Rewoldt,W. M. Tang, and M. S. Chance, Physics of Fluids **25**, 480 (1982).

[14]G. Rewoldt, W. M. Tang, and R. J. Hastie, Physics of Fluids **30**, 807 (1987).

[15]G. Rewoldt, L. Ku, W. M. Tang, and W. A. Cooper, Physics of Plasmas **6**, 4705 (1999).

[16]G. Rewoldt, L. Ku, and W. M. Tang, Physics of Plasmas **12**, 102512 (2005).

[17]P. Xanthopoulos, F. Merz, T. Goerler, and F. Jenko, Physical Review Letters **99**, 035002 (2007).

[18]T. Watanabe, H. Sugama, and S. Ferrando-Margalet, Nuclear Fusion **47**, 1383 (2007).

[19]W. Dorland, F. Jenko, M. Kotschenreuther, and B. N. Rogers, Physical Review Letters **85**, 5579 (2000).

[20]G. G. Howes, S. C. Cowley, W. Dorland, G. W. Hammett, E. Quataert, and A. A. Schekochihin, The Astrophysical Journal **651**, 590 (2006).

[21]S. P. Hirshman, U. Schwenn, and J. Nhrenberg, Journal of Computational Physics **87**, 396 (1990).

[22]S. P. Hirshman and D. K. Lee, Computer Physics Communications **39**, 161 (1986).

[23]A. H. Boozer, Physics of Fluids **23**, 904 (1980).

[24]D. V. Anderson, Int. J. Supercomput. Appl. **4**, 34 (1990).

[25]A. Cooper, Plasma Physics and Controlled Fusion **34**, 1011 (1992).

[26]W. Guttenfelder, J. Lore, D. T. Anderson, F. S. B. Anderson, J. M. Canik, W. Dorland, K. M. Likin, and J. N. Talmadge, Physical Review Letters **101**, 215002 (2008).

[27]M. Kotschenreuther, G. Rewoldt, and W. M. Tang, Computer Physics Communications **88**, 128 (1995).

[28]C. Bourdelle, W. Dorland, X. Garbet, G. W. Hammett, M. Kotschenreuther, G. Rewoldt, and E. J. Synakowski, Physics of Plasmas **10**, 2881 (2003).

[29]A. Reiman, L. Ku, D. Monticello, S. Hirshman, S. Hudson, C. Kessel, E. Lazarus, D. Mikkelsen, M. Zarnstorff, L. A. Berry, A. Boozer, A. Brooks, W. A. Cooper, M. Drevlak, E. Fredrickson, G. Fu, R. Goldston, R. Hatcher, M. Isaev, C. Jun, S. Knowlton, J. Lewandowski, Z. Lin, J. F. Lyon, P. Merkel, M. Mikhailov, W. Miner, H. Mynick,

G. Neilson, B. E. Nelson, C. Nuhrenberg, N. Pomphrey, M. Redi, W. Reiersen, P. Rutherford, R. Sanchez, J. Schmidt, D. Spong, D. Strickler, A. Subbotin, P. Valanju, and R. White, Physics of Plasmas **8**, 2083 (2001).

[30]L. Ku and A. H. Boozer, Nuclear Fusion **50**, 125005 (2010).

[31]G. Rewoldt and W. M. Tang, Physics of Fluids B: Plasma Physics **2**, 318 (1990).

[32]J. Y. Kim, W. Horton, D. I. Choi, S. Migliuolo, and B. Coppi, Physics of Fluids B: Plasma Physics **4**, 152 (1992).

[33]F. Jenko, W. Dorland, M. Kotschenreuther, and B. N. Rogers, Physics of Plasmas **7**, 1904 (2000).

[34]P. Xanthopoulos, W. A. Cooper, F. Jenko, Y. Turkin, A. Runov, and J. Geiger, Physics of Plasmas **16**, 082303 (2009).

[35]M. Barnes, *Trinity: A Unified Treatment of Turbulence, Transport, and Heating in Magnetized Plasmas*, Ph.D. thesis, University of Maryland (2009).

FIGURES

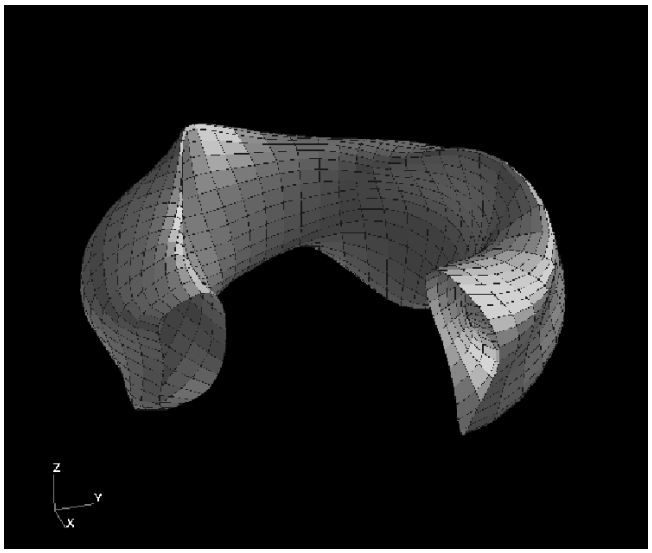

FIG. 1. Equilibrium of NCSX design QAS3-C82 which is quasi-axisymmetric and has 3 field periods.

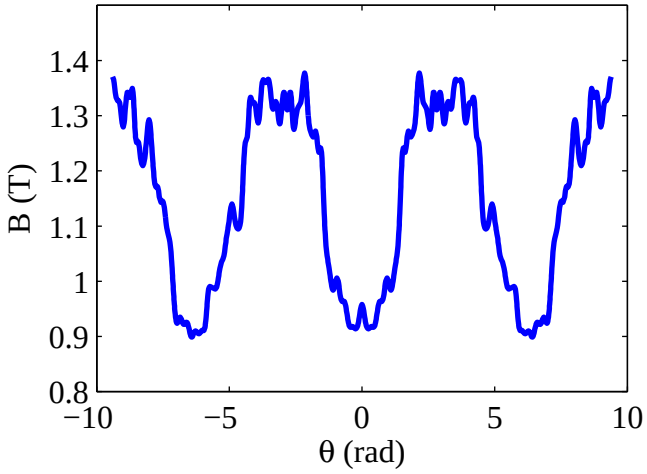

FIG. 2. Standard B vs. θ grid for QAS3-C82, with $s = 0.875$, $\alpha = \pi/3$, and $\theta_0 = 0$.

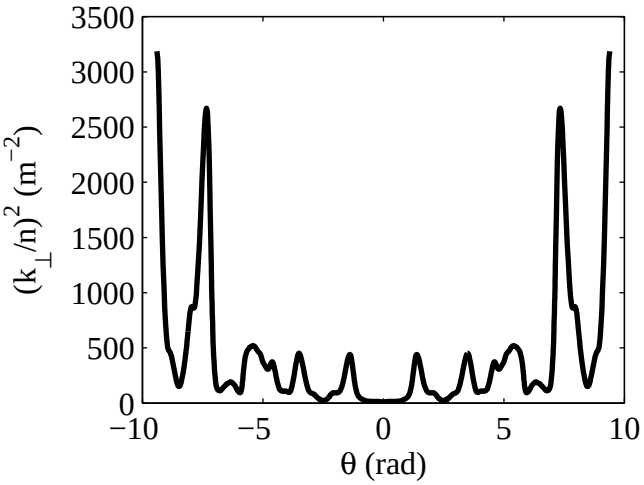

FIG. 3. Variation of $(\frac{k_\perp}{n})^2(\theta)$ for QAS3-C82, with $s = 0.875$, $\alpha = \pi/3$, and $\theta_0 = 0$.

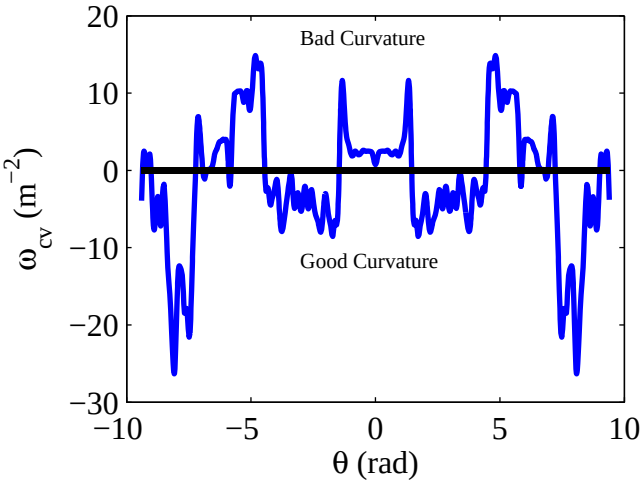

FIG. 4. Variation of the curvature drift frequency ($\omega_{cv} = (\mathbf{k}_\perp/n) \cdot \mathbf{b} \times [\mathbf{b} \cdot \nabla \mathbf{b}]$) (for $n = 1$) along θ for QAS3-C82, with $s = 0.875$, $\alpha = \pi/3$, and $\theta_0 = 0$.

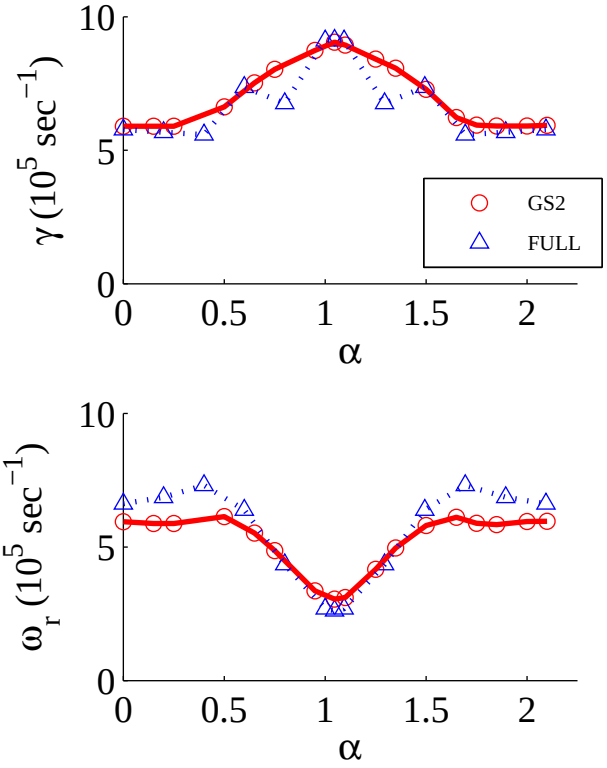

FIG. 5. (color online) Variation of γ and ω_r with α at constant $s = 0.875$ and $\theta_0 = 0$ with $\eta_i = \eta_e = 3$ and $k_y\rho_i(\alpha = \frac{\pi}{3}) = 0.3983$.

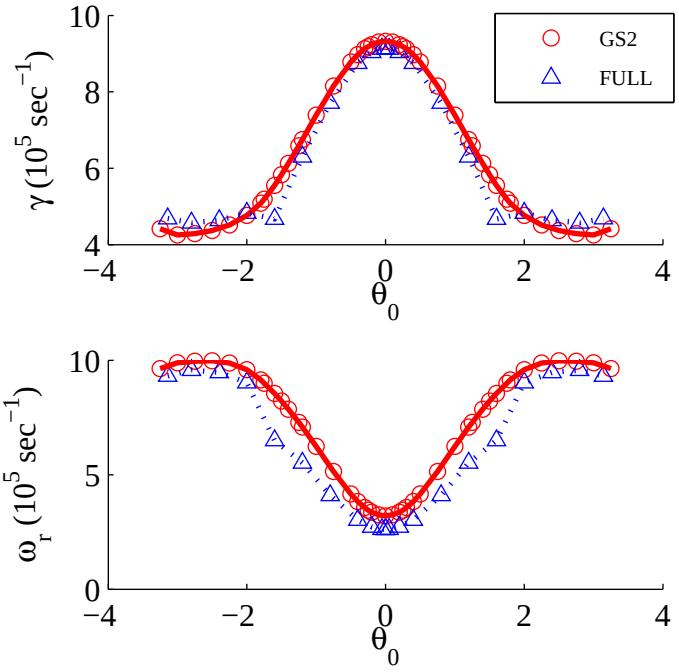

FIG. 6. (color online) Variation of γ and ω_r with θ_0 at constant $s = 0.875$ and $\alpha = \pi/3$ with $\eta_i = \eta_e = 3$ and $k_y\rho_i = 0.3983$.

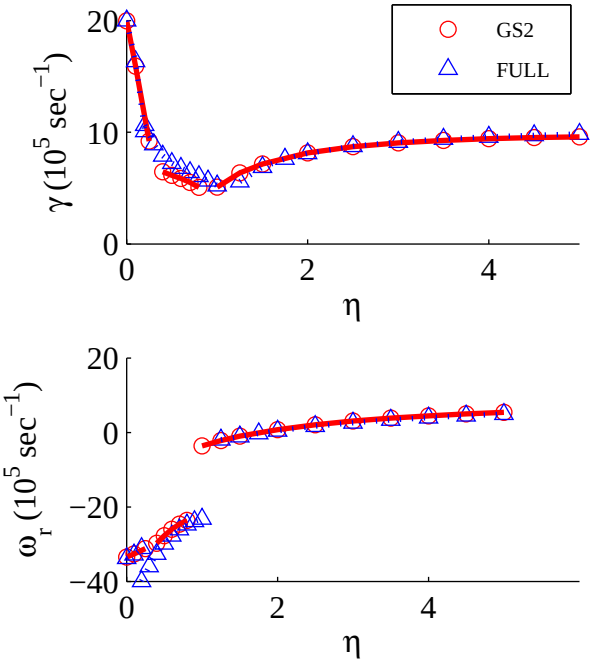

FIG. 7. (color online) Variation of γ and ω_r with $\eta_i = \eta_e$ with $k_y\rho_i = 0.3983$.

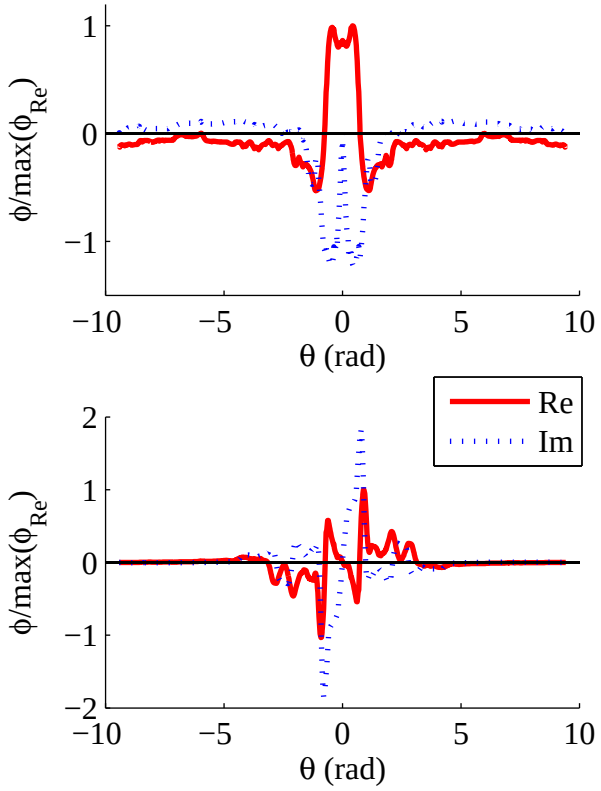

FIG. 8. (color online) Variation of the normalized GS2 eigenfunctions of electrostatic, collisionless toroidal drift modes along the field line at $\eta = 3$ (top figure) and at $\eta = 0.5$ (bottom figure) with $k_y \rho_i = 0.3983$.

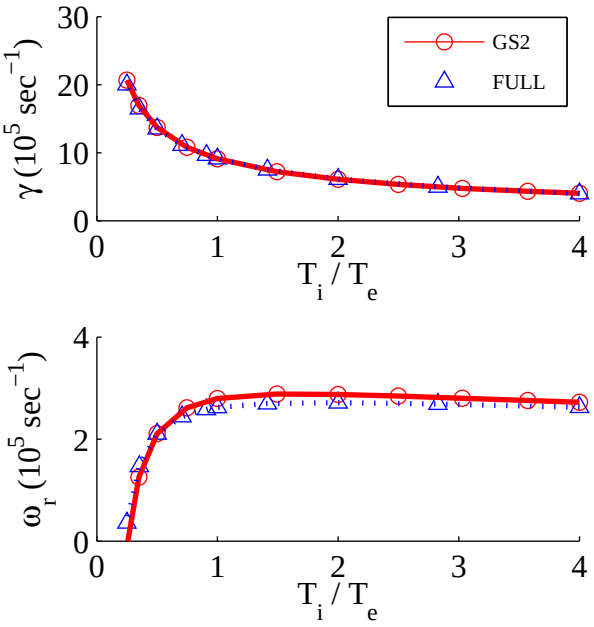

FIG. 9. (color online) Variation of γ and ω_r with T_i/T_e with $k_y\rho_i = 0.3983$ and $\eta_i = \eta_e = 3$.

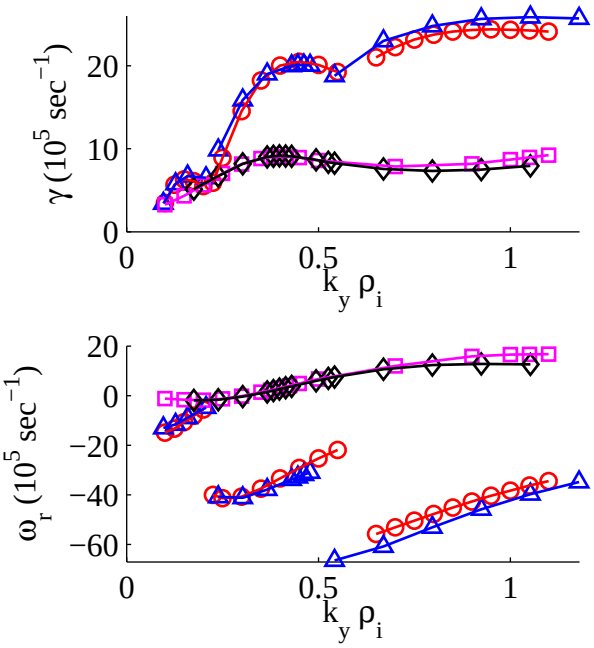

FIG. 10. (color online) Variation of γ and ω_r with $k_y\rho_i$. Circles: GS2, $\eta = 0$; triangles: FULL, $\eta = 0$; squares: GS2, $\eta = 3$; diamonds: FULL, $\eta = 3$.

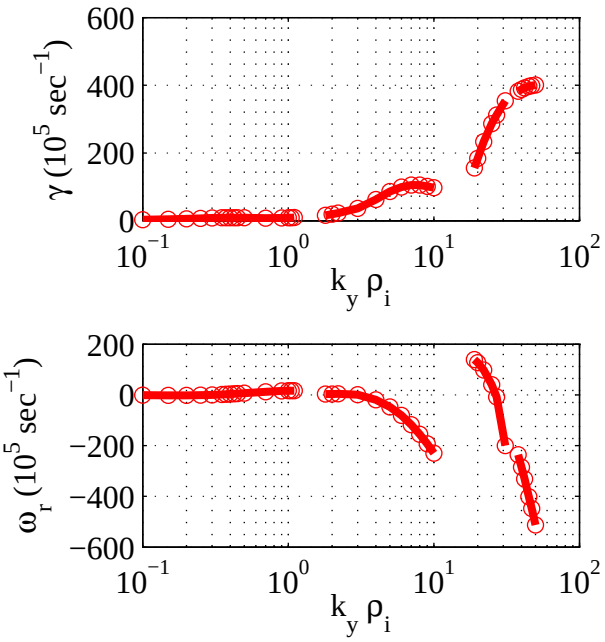

FIG. 11. (color online) Extended variation from GS2 of γ and ω_r with $k_y\rho_i$ and $\eta_i = \eta_e = 3$.

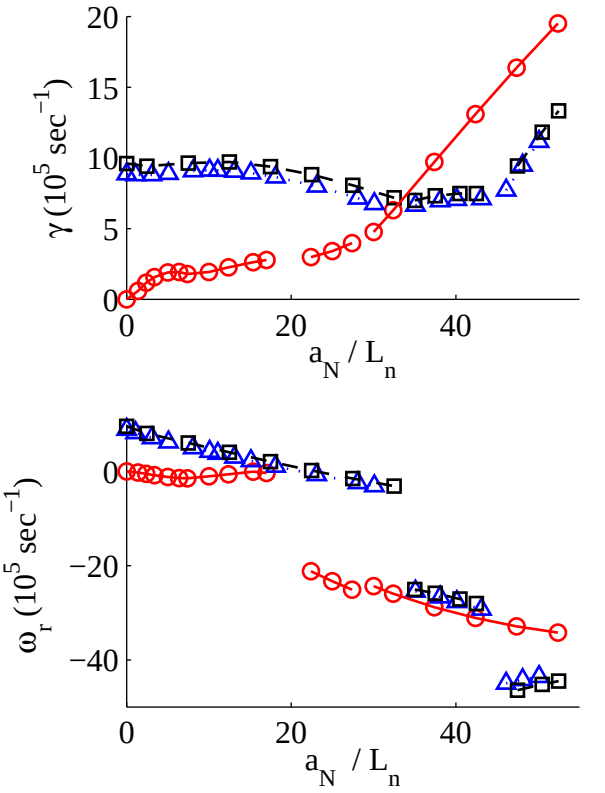

FIG. 12. (color online) Variation of γ and ω_r with a_N/L_n with $k_y\rho_i = 0.3983$. Circles: $a_N/L_T = 0.0$; triangles: $a_N/L_T = 39.3$; squares: $a_N/L_T = 44.9$.

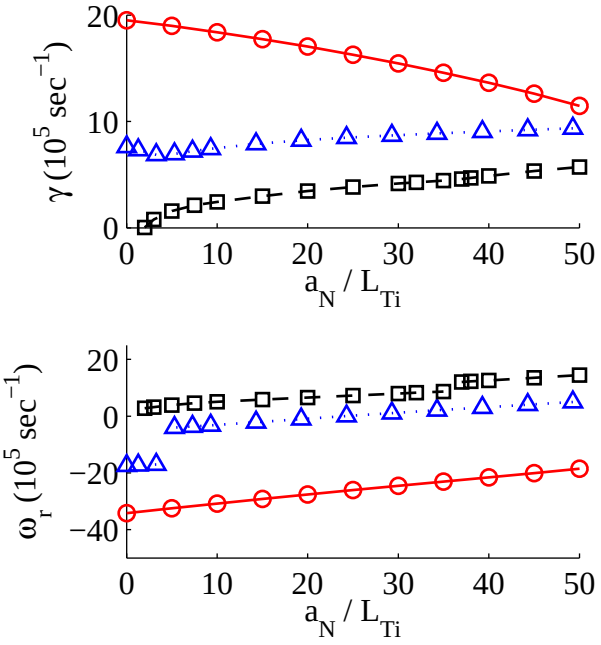

FIG. 13. (color online) Variation from GS2 of γ and ω_r with a_N/L_{Ti} with $k_y\rho_i = 0.3983$. Circles: $a_N/L_n = 52.4, a_N/L_{Te} = 0.0$; triangles: $a_N/L_n = 13.1, a_N/L_{Te} = 39.3$; squares: $a_N/L_n = 0.0, a_N/L_{Te} = 0.0$.

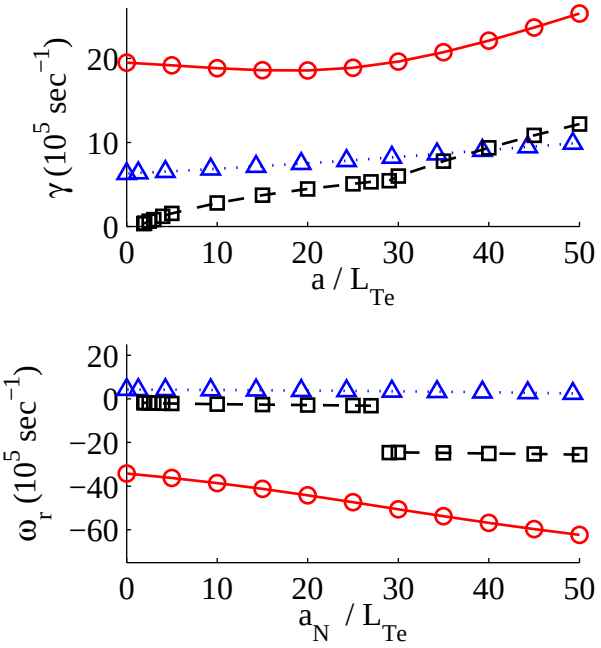

FIG. 14. (color online) Variation from GS2 of γ and ω_r with a_N/L_{Te} for the case of Fig. 2 with $k_y\rho_i = 0.3983$. Circles: $a_N/L_n = 52.4, a_N/L_{Ti} = 0.0$; triangles: $a_N/L_n = 13.1, a_N/L_{Ti} = 39.3$; squares: $a_N/L_n = 0.0, a_N/L_{Ti} = 0.0$.

TABLES

$s \approx (\langle r/a \rangle)^2$	0.875
$\alpha = \zeta - q\theta$	$\pi/3$
θ_0	0
q	2.118
$\langle\beta\rangle$	0.01%
$k_y\rho_i$	$0.3983 (n = 25)$
$T_i = T_e$	$1keV$
$\eta_i = \eta_e$	3
$a_N/L_{ni} = a_N/L_{ne}$	≈ 13.096
$a_N/L_{Ti} = a_N/L_{Te}$	≈ 39.288

R	$\approx 4a_N \approx 1.4m$
$a_N = (\frac{n}{k_\perp(\theta=0,\theta_0=0)})$	$\approx 0.352m$
$B_a = \langle B \rangle$	$1.15T$
m_{ref}	$2m_p$
v_t	$\sqrt{(eT_i 1000)/m_{ref}}$
GS2 ω units v_t/a_N	$\approx 6.214 \times 10^5 sec^{-1}$

TABLE I. The set of local parameters used in a standard case microinstability simulation based on the QAS3-C82 equilibrium. Note: a_N is not the minor radius; it is discussed in App. A.